

The Fornax Cluster VLT Spectroscopic Survey. I – VIMOS spectroscopy of compact stellar systems in the Fornax core region

V. Pota^{1*}, N. R. Napolitano¹, M. Hilker², M. Spavone¹, C. Schulz², Michele Cantiello³, C. Tortora⁴, E. Iodice¹, M. Paolillo^{5,13}, R. D’Abrusco⁶, M. Capaccioli⁵, T. Puzia¹⁰, R. F. Peletier⁴, A. J. Romanowsky⁷, G. van de Ven², C. Spinelli¹, M. Norris⁹, T. Lisker⁸, R. Munoz¹⁰, P. Schipani¹, P. Eigenthaler^{10,11}, M. A. Taylor¹², R. Sánchez-Janssen¹⁴, Y. Ordenes-Briceño^{8,10}

¹ INAF – Osservatorio Astronomico di Capodimonte, Salita Moiariello, 16, 80131 - Napoli, Italy

² European Southern Observatory, Karl-Schwarzschild-Straße 2, 85748 Garching bei München, Germany

³ INAF – Astronomical Observatory of Abruzzo, Via Maggini, 64100, Teramo, Italy

⁴ Kapteyn Astronomical Institute, University of Groningen, PO Box 800, 9700 AV Groningen, The Netherlands

⁵ Dipartimento di Fisica Ettore Pancini, Università di Napoli Federico II, via Cintia, 80126 - Napoli Italy

⁶ Harvard-Smithsonian Center for Astrophysics, 60 Garden St., Cambridge (MA), 02138, US

⁷ University of California at Santa Cruz, Astronomy and Astrophysics Department, US

⁸ Astronomisches Rechen-Institut Zentrum für Astronomie Mönchhofstraße 12-14 69120 Heidelberg, Germany

⁹ Jeremiah Horrocks Institute, University of Central Lancashire, Preston, PR1 2HE, United Kingdom

¹⁰ Pontificia Universidad Católica de Chile, Av. Vicuña Mackenna 4860, Santiago, Chile

¹¹ CASSACA, Camino El Observatorio 1515, Las Condes, Santiago, Chile

¹² Gemini Observatory, Northern Operations Center, 670 North A'ohoku Place, Hilo, HI 96720, USA

¹³ INFN, Sezione di Napoli, via Cintia, 80126, Napoli, Italy

¹⁴ UK Astronomy Technology Centre, Royal Observatory Edinburgh, Blackford Hill, Edinburgh, EH9 3HJ, U

7 March 2018

ABSTRACT

We present the results of a wide spectroscopic survey aimed at detecting extragalactic globular clusters (GCs) in the core of the Fornax cluster. About 4500 low resolution spectra (from 4800 to 10000 Å) were observed in 25 VLT/VIMOS masks covering the central 1 deg² around the dominant galaxy NGC 1399 corresponding to \sim 175 kpc galactocentric radius. We describe the methodology used for data reduction and data analysis. We found a total of 387 unique physical objects (372 GCs and 15 ultra compact dwarfs) in the field covered by our observations. Most of these objects are associated with NGC 1399, with only 10% likely belonging to other giant galaxies. The new VIMOS dataset is complementary to the many GC catalogues already present in the literature and it brings the total number of tracer particles around NGC 1399 to more than 1130 objects. With this comprehensive radial velocity sample we have found that the velocity dispersion of the GC population (equally for red and blue GC populations) shows a relatively sharp increase from low velocity dispersion (\sim 250 – 350 km s⁻¹) to high velocity dispersion (\sim 300 – 400 km s⁻¹) at projected radius of \approx 10 arcmin (\sim 60 kpc) from the galaxy centre. This suggests that at a projected radius of \approx 60 kpc both blue and red GC populations begin to be governed by the dominating Fornax cluster potential, rather than by the central NGC 1399 galaxy potential. This kinematic evidence corroborates similar results found using surface brightness analysis and planetary nebulae kinematics.

Key words: galaxies:star clusters – galaxies:evolution – galaxies: kinematics and dynamics

1 INTRODUCTION

Nearby galaxy clusters are ideal laboratories for studying the evolution of low and high mass galaxies as well as dense stellar sys-

* E-mail: vincenzo.pota@gmail.com

tems (globular clusters, compact dwarf galaxies, planetary nebulae, etc.) in dense environments. The Virgo and Fornax clusters are the closest galaxy clusters, hence providing privileged targets where detailed observations of the galaxy and small stellar system content can be performed, and galaxy formation theories can be tested (e.g., Strader et al. 2011).

The Fornax cluster is the most massive galaxy overdensity after the Virgo cluster within 20 Mpc and it is an ideal target to study the effect of the environment on the structure and assembly of galaxies of any type, from the massive central giant early-type systems to the dwarf galaxies (e.g., Ferguson & Sandage 1989; Muñoz et al. 2015; Iodice et al. 2016; Venhola et al. 2017; Eigenthaler et al. 2018). Despite its regular appearance, it has been found that the assembly of Fornax is still ongoing. Although its core seems in an evolved phase (Grillmair et al. 1994; Jordán et al. 2007) and most of the bright ($m_B < 15$ mag) cluster members are early-type galaxies (Ferguson & Sandage 1989), the presence of stellar and GC tidal streams (e.g. Iodice et al. 2016, D’Abrusco et al. 2016, Eisenhardt et al. 2017) have revealed that there are still signs of active galaxy interactions in the region inside 200 kpc, which mirrors the large scale activity, including the accretion of the Fornax-A (NGC 1316) subgroup (dominated by the brightest cluster member, NGC 1316) into the cluster core along a cosmic web filament (Drinkwater et al. 2000; Scharf et al. 2005).

To kinematically map the complexity of the cluster core out to at least 200 kpc using discrete kinematical tracers (e.g. GCs, UCDs and PNe) and finally connect the large scale kinematics down to the scale of the dwarf galaxies, we have started a multi-instrument observational effort called the Fornax Cluster VLT Spectroscopic Survey (FVSS). As a part of this effort we have acquired integral field spectroscopy of dwarfs galaxies (see Mentz et al. 2016, Spinelli et al. in preparation), a counter dispersed imaging run with FORS2 to detect and measure radial velocities of planetary nebulae (Spinelli et al. 2018, submitted as FVSS II) and multi-object spectroscopy of GC and UCD candidates with VIMOS/VLT.

The latter program is the topic of this paper, where we present the radial velocity catalogue of GCs and UDGs in the core of Fornax, which is complementary to archival spectroscopic GC datasets on a more limited area: Schuberth et al. (2010) (which incorporates the catalogue of Dirsch et al. 2004), Bergond et al. (2007) and other catalogues discussed throughout the text. The novelty of the sample discussed in this paper is the uniform coverage of the central 1 deg² of the Fornax core which allows us to provide a spatially complete map of the kinematics of the galaxies in the field out to the regions where they meet the intracluster field (see e.g., Napolitano et al. 2003; Arnaboldi et al. 2012). Here, dynamical times are longer than the central galaxy regions and we expect to find the kinematical signature of the substructures already seen in the FDS photometry (Iodice et al. 2016) or other gravitational interactions such as shells and tidal tails in the kinematics of the galaxy outskirts or intracluster regions (Napolitano et al. 2002, 2003; Murante et al. 2007; Bullock & Johnston 2005; Rudick et al. 2006; Duc et al. 2011; Longobardi et al. 2015). FVSS will be the foundation of a multifaceted project to constrain the baryonic and dark mass distribution in the core of the Fornax cluster with high precision, thus shedding light on the assembly history of massive galaxies in one of the nearest dense environments.

In this first paper of the series, we present the radial velocity catalogue of GCs. The assumed distance is 19.95 Mpc (Tonry et al. 2001). Hence, 1 arcmin ~ 5.8 Kpc.

The paper is structured as follows: Section 2 describes the data acquisition and reduction. The redshift estimation is discussed

in Section 3.1, results are presented in Section 4 and discussed in Section 5. We summarise the results of the paper and conclude in Section 6.

2 DATA

This Section discusses all the steps undertaken to compile the spectroscopic catalogue discussed in this paper. The photometric surveys that constitute the input of our spectroscopic work are briefly described in §2.1. The workflow consists of selecting a sample of GC candidates based on photometric selection criteria (§2.2) and then using the derived sample to design multi-object masks (§2.3) for follow-up observations (§2.4).

2.1 Photometry

2.1.1 The Fornax Deep Survey

The Fornax Deep Survey¹ (FDS) is a joint project based on Guaranteed Time Observation surveys, FOCUS (P.I. R. Peletier) and VEGAS (P.I. E. Iodice, Capaccioli et al. 2015), aimed at studying the formation and assembly of the Fornax Cluster out to its virial radius with a variety of observations. These include deep photometry, supplemented by cross-match with other wavelength observations such as X-rays (Paolillo et al. 2002, e.g.,) and multi-object and integral-field spectroscopy. The cornerstone of FDS is deep multiband (u, g, r and i) imaging data from the OmegaCam (Kuijken 2011) camera at the VLT Survey Telescope (VST, Schipani et al. 2012), covering an area of ~ 30 deg² of the cluster out to the virial radius. The area includes the Fornax-A subgroup, hence providing a full coverage of the cluster structure under assembly. The depth of the imaging dataset reaches ~ 30 mag/arcsec² in the g -band (Iodice et al. 2016, 2017), among the deepest acquired on the cluster so far (Venhola et al. 2017). VISTA/VIRCAM observations in J and K (with limiting magnitudes $K_s = 23.4$ AB mag, and $J = 23.4$ AB mag, respectively) are also available (see e.g. Muñoz et al. 2015), to complement the optical data and optimise galaxy and globular cluster membership and the selection of follow-up targets (e.g. globular clusters, GCs hereafter, and/or ultra compact dwarf galaxies, UCDs hereafter).

The multi-band deep images have been used to study the light distribution and colours of cluster galaxies out to 8–10 effective radii and beyond to characterise the faint galaxy haloes. These studies revealed the presence of ultra-faint stellar structures in the core of Fornax: fingerprints of past and ongoing interaction between galaxies falling into the deep potential well of the cluster (Iodice et al. 2016; Venhola et al. 2017). The same conclusion is backed up by the complex distribution of globular clusters in the Fornax cluster (D’Abrusco et al. 2016; Cantiello et al. 2017).

2.1.2 Next Generation Fornax Survey

The Next Generation Fornax Survey (NGFS; Muñoz et al. 2015, Puzia et al. 2018, in prep.) is an optical and near-infrared imaging survey of the Fornax galaxy cluster virial sphere ($R_{\text{vir}} \sim 1.4$ Mpc; Drinkwater et al. 2001). NGFS uses the Dark Energy Camera (DE-Cam; Flaugher et al. 2015) mounted on the 4-meter Blanco telescope at Cerro Tololo Interamerican Observatory (CTIO) in the optical wavelengths and the European Southern Observatory (ESO)

¹ ESO programme ID (094.B-0687)

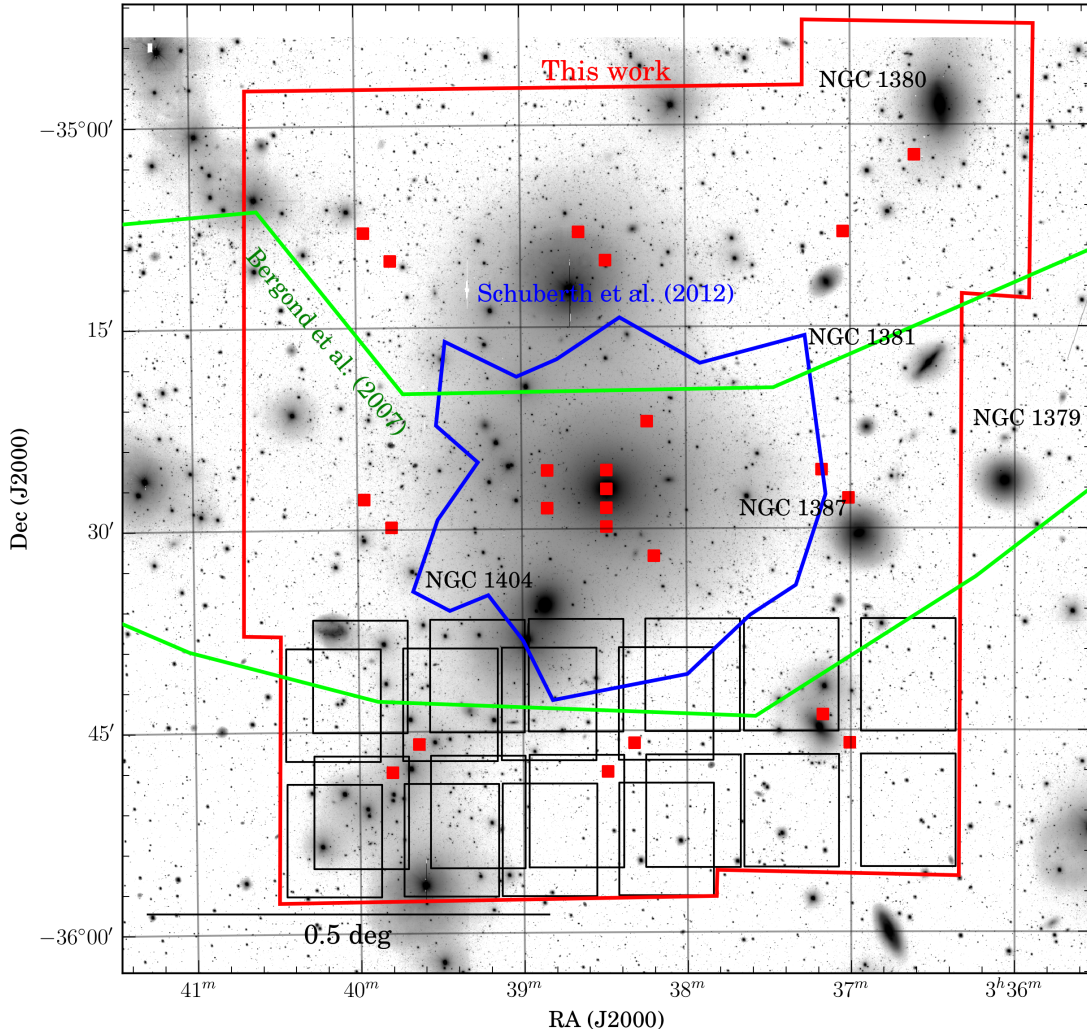


Figure 1. Layout of the observations. The background image is a mosaic of several VST/OmegaCAM pointings in the g -band. The central galaxy is NGC 1399. Additional Fornax galaxies are also labeled. The red boxes mark the centers of all 25 VIMOS pointings. The footprints of some VIMOS masks are shown on the bottom for illustrative purposes. Note how the VIMOS masks are dithered to maximize spatial coverage. The region covered by all 25 VIMOS is outlined in red, whereas the regions covered by literature studies are shown in green (Bergond et al. 2007) and blue (Schuberth et al. 2010).

3.7-meter VISTA telescope with VIRCam (Sutherland et al. 2015) for near-infrared observations. The current NGFS survey footprint covers $\sim 50 \text{ deg}^2$ with 19 DECam tiles of 2.65 deg^2 each, and detects point-sources at $S/N = 5$ down to $u' = 26.5 \text{ mag}$, $g' = 26.1 \text{ mag}$, $i' = 25.3 \text{ mag}$, $J = 24.0 \text{ mag}$ and $K_s = 23.4 \text{ mag}$. Here we make use of preliminary NGFS K_s -band point source catalogs.

The panchromatic NGFS data were recently used to detect low surface-brightness galaxies (Muñoz et al. 2015), measure the morphological, scaling, and clustering properties of more than 600 dwarf galaxies (Eigenthaler et al. 2018, rdenes-Briceo et al. 2018a, submitted), study their nucleation and stellar population properties (rdenes-Briceo et al. 2018b, submitted, Eigenthaler et al. 2018b, submitted), and analyze the globular cluster systems in Fornax (Írdenes-Briceo et al. 2018c, submitted).

2.2 Selection of globular cluster candidates

The selection of GC candidates was based on VST/OmegaCAM photometry in the de-reddened g and i band from the FDS (D'Abrusco et al. 2016; Iodice et al. 2016) and preliminary VISTA/VIRCAM photometry in the K_s band from the NGFS. In the combined 2-colour giK_s diagram, confirmed GCs from Schuberth et al. (2010) are confined to a restricted colour-colour space. We defined a polygon around the radial velocity members in this colour space, which serves as first order selection criterion for our GC candidates.

As an additional criterion we used the published wide-field Washington photometry from Dirsch et al. (2004) and Bassino et al. (2006) to construct a $C - i$ vs. $i - K_s$ diagram. Since the Washington C -band is similar to a u -band filter and the uiK_s plane is a very powerful tool to discriminate GCs from foreground and background objects (Muñoz et al. 2014), the CiK_s plane is the cleanest selection criterion. Unfortunately, the spatial coverage of the Washington photometry is not complete in the central square degree due to chip gaps and the restricted field-of-view. Out of the 1065 unique

spectroscopic targets with CiK_s photometry, 809 (or $\sim 76\%$) are within this selection polygon.

As shown in Sect. 2.2, the final mask design resulted in slit allocations on 4340 unique spectroscopic targets. 4321 of those have giK_s photometry, and 2643 (or $\sim 61\%$) of them are contained in the selection polygon defined for potential GCs in the giK_s space. We note that the missing u-band information in this colour space leads to a high fraction of contaminating foreground stars and background galaxies (see Sect. 3.1).

Here, we applied a magnitude restriction of $17.0 < i < 23.0$ mag to our GC candidate sample in order to avoid severe contamination by foreground stars at bright magnitudes and too low signal-to-noise spectra at the faint magnitudes. For the very central regions of NGC 1399, which are dominated by the galaxy light, we found additional GC candidates taking advantage of the more accurate photometry and morphological classification derived from *Hubble Space Telescope/ACS* data by Puzia et al. (2014).

Finally, all other allocated fibers, i.e. the remaining 1678 slits, besides a small portion used to duplicate targets, were split to observe known stars and background galaxies. These latter will be discussed in a separate paper.

The FDS gi , the NGFS K_s , Washington C , as well as the central ACS photometric catalogs, were matched with SExtractor photometry of point and extended sources in all pre-images (ESO programme 094.B-0687), which were taken in R -band prior to the spectroscopic observations. The x and y coordinates of sources in the pre-images are needed to create VIMOS catalogs for the creation of mask files with the VMMPS (VIMOS Mask Preparation Software, Bottini et al. 2005) from ESO.

2.3 VIMOS pointings and mask design

A total of 25 VIMOS masks were designed covering the central square degree around NGC 1399. The mask pointings were micro-dithered in such a way that the gaps between the four VIMOS CCDs (or quadrants) were covered by the adjacent mask.

In Figure 1 we show the spatial distribution of the VIMOS pointings, along with the footprints of archival observations in the same sky region from Schuberth et al. (2010) and Bergond et al. (2007). It is clear that the mask distribution is much more homogeneous with respect to previous studies, although our target sampling varies across the field. Besides the central giant elliptical NGC 1399, the total covered area contains other giant galaxies, i.e., NGC 1404, NGC 1387 and NGC 1380. Figure 2 shows how the 2-dimensional density of allocated slits is considerably higher in the center with respect to the outskirts. Eight of the 25 pointings were dedicated to the central 25×25 arcmin 2 to account for the higher density of GC candidates close to NGC 1399.

The use of the MR grism allows a multiplexing of two in wavelength direction (parallel to declination), i.e. spectra are not overlapping if slits are placed close to the bottom and top of the chip areas in all quadrants. For a first automatic slit allocation we used VMMPS with a catalog of GC candidates from the giK_s selection as input. Since the result of the automatic slit allocation was not satisfactory, we optimized the slit allocation of targets manually, for example by de-centering some targets in the slits while still keeping enough sky, or by allowing some overlap in wavelength range for multiplexed spectra, and by giving preference to targets that also fulfill the CiK_s selection criterion. The remaining free area on the chips was then filled with slits centered on GC candidates from the $(g - i)$ colour selection or on pre-selected background galaxies to allow ancillary science on photometric redshift confirmations.

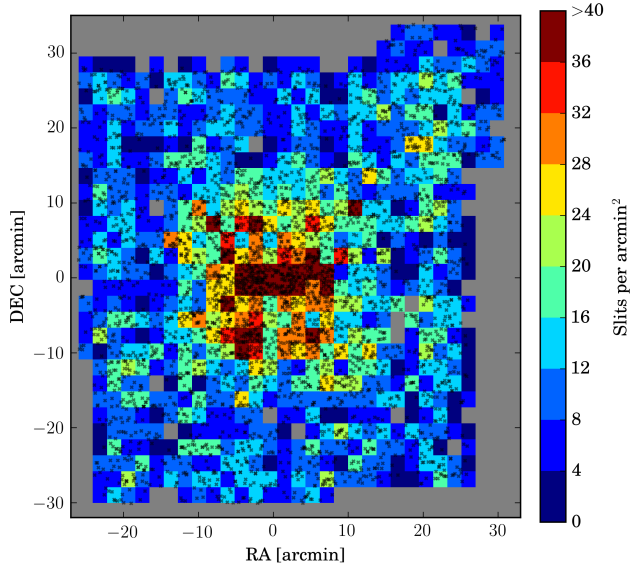


Figure 2. Two dimensional spatial density of VIMOS slits. Slits are shown as small black crosses, whereas the colours represent total counts in boxes of 2×2 arcmin 2 . Axes express the distance in arcmin from NGC 1399. More slits were placed towards the center of the cluster, where the target density is higher. North is toward the top, East to the left.

In this way, we defined 4574 slits in total for the 25 pointings ranging from 157 to 202 slits per pointing (or 36 to 60 slits per quadrant). Several slits were positioned in such a way to cover more than one target if they had the same declination and a small distance in right ascension (of the order of 10 arcsec or less). Since the fields are overlapping, about 300 targets have been observed twice and four targets even three times through different masks. This allows us to better understand uncertainties in the radial velocity measurements and correct for them between different masks. Discounting all duplications, we ended up with about 4340 unique targets for which spectra were taken.

2.4 Observations

Spectroscopic observations were carried out with the VIable MultiObject Spectrograph (VIMOS, Le Fèvre et al. 2003), mounted on the VLT-UT3 Melipal telescope at the ESO Paranal observatory in Chile and used in multi-object mode. Data were acquired in Period 94 (Program ID: 094.B-0687, PI: M. Capaccioli), from October 2014 to January 2015. The VIMOS spectrograph was equipped with a filter CG475, which cuts off wavelengths bluer than 4750 Å, and a MR grating with a spectral resolution $R = 580$ (or 12.0 Å FWHM) and a dispersion of 2.5 Å pix. All slits had a width of 1 arcsec. The pixel scale in the spatial direction was 0.205 arcsec/pix. This setup allows us to explore the spectral window ranging from 4800 to 10000 Å. Sky transparency was set to clear.

VIMOS is equipped with four CCDs, arranged in four quadrants with chip gaps of ~ 2 arcmin in vertical and horizontal direction (see examples of the VIMOS detector footprints in Figure 1). Overall, one VIMOS mask set covers a field of $4 \times (7 \times 8$ arcmin 2). All masks were observed for 1.5 hours in total, divided into three dithered exposures of 30 minutes. The seeing ranged

from 0.66 arcsec to 1.15 arcsec, with a median of 0.85 arcsec. The median airmass was 1.061.

2.5 Data reduction

The reduction of the VIMOS data was performed using the Reflex environment (Freudling et al. 2013) of the ESO VIMOS pipeline. For each VIMOS pointing, the data consist of the scientific images, flat fields and arc lamp calibration images taken immediately after the science exposures. Each science exposure has a distribution of slits containing the science spectra of the targets. Indeed every slit is also contaminated by the emission spectrum of the earth's atmosphere. Since the wavelengths of the sky emission lines are precisely known they can be used for the absolute wavelength calibration of the spectra.

In order to obtain the final wavelength calibrated science spectra, we proceeded as follows. First, a wavelength calibration is performed using the provided arc lamp spectrum. Second, we calculated the residual shift of the sky emission lines with respect to their rest frame wavelength. For this purpose we provided our own sky line catalog, in which the wavelengths of prominent sky lines, in particular in the Ca triplet (CaT) region, are listed. The pipeline determines this shift for each spectrum in each science exposure individually, which is essential because the wavelength shifts are not the same for the three exposures: the shift is largest for the first exposure and smallest for the third exposure. This is caused by the change of instrument flexure between the first science exposure and the final arc lamp exposure. In other words, the third science exposure is taken closest in time, i.e. under almost the same instrument conditions to the arc lamp exposure, and thus its wavelength calibration is the most accurate. Finally, the pipeline stacks the three individual science exposures and extracts sky subtracted object spectra from the combined science frame.

Unfortunately, the pipeline does not apply the wavelength shifts to the individual spectra before the stacking, meaning that the stacked spectra are not corrected for the residual shifts. This leads to an incorrect absolute wavelength calibration and also to a slight line broadening in the stacked spectra. Even though we cannot correct for the line broadening with the current ESO pipeline version, we found a workaround to correct for the absolute wavelength calibration of the spectra, which is necessary for an accurate measurement of the radial velocities of the objects. To zero-th order, it can be assumed that the median wavelength shift in the stacked spectrum is the same as the one derived for the second exposure. Thus, we re-reduced the second science exposure of all available data to determine the median wavelength shift in each multiplex of each mask by taking the average shift of all spectra in that multiplex. Then, the wavelength of each stacked spectrum was shifted by an amount as determined by the multiplex and the mask in which the spectrum is located. All further analyses were carried out on the spectra corrected in this way.

For each mask, the REFLEX pipeline outputs multi-extension fits files which include the calibrated 2D spectra, the calibrated 1D spectra (and respective errors) and a 2D model of the sky lines. To make the dataset more manageable, we implemented a *python/astropy* (The Astropy Collaboration et al. 2018) script which copies different data structures corresponding to each slit into a multi-extension fits file. Each slit is associated to a fits file which contains: the 1D scientific spectrum, the 1D error spectrum, the sky-subtracted, wavelength-corrected 2D spectrum and a thumbnail of the object of 5×5 arcsec 2 from *g*-band VST imaging.

3 ANALYSIS

3.1 Redshift estimation

A total of 6700 spectra were extracted by the REFLEX pipeline. The number of spectra is larger than the number of slits because multiple spectra can be extracted from one slit. These spectra belong to objects genuinely associated with the Fornax cluster (i.e., GCs, UCDs or dwarf galaxies), as well as Galactic stars, background galaxies and sources with signal-to-noise (S/N) too low to be classified with certainty.

Radial velocities were computed with *iraff/fxcor*, which performs cross-correlation between the Fourier-transformed scientific spectrum and a Fourier-transformed set of template spectra (Tonry & Davis 1979). *Fxcor* was preferred to full spectra fitting approaches (e.g. pPXF, Cappellari & Emsellem 2004) because the former does not require initial guesses on the radial velocity and it is more CPU efficient.

The Indo-U.S. Library of Coudé Feed Stellar Spectra (Valdes et al. 2004) was used as library of template spectra. The library contains 1273 stellar spectra, observed with a dispersion of 0.44 Å/pix and a resolution of ~ 1 Å. The spectra cover the 3460 – 9464 Å range, which overlaps adequately with the wavelength range of our VIMOS spectra. From the whole library, we selected a random subset of 40 stars with spectral types from *F* to *M* because this is the range expected for metal-poor to metal-rich GCs.

The 40 stellar spectra were convolved with a Gaussian filter of standard deviation $\sigma = 12.0\text{Å} / 2.355$, where 12.0 Å is the FWHM resolution of our VIMOS spectra and 2.355 is the constant relating the FWHM with σ .

The scientific spectra were prepared as follows. First, we computed the median signal-to-noise per resolution element S/N , where the signal S is measured in the range 5000–6600 Å and the noise N is the noise returned by the REFLEX pipeline in the same wavelength range. Second, telluric bands in the range 6850 – 7688 Å and some bright skyline regions skylines were replaced with the fit to the spectral continuum. The continuum was computed with *iraf/continuum* by averaging ten contiguous pixels and interpolating the result with a cubic spline coupled with a 3σ rejection algorithm.

Naively, one may think that cross-correlating the full wavelength range of our VIMOS spectra will return more robust radial velocities because the number of atomic lines used for the convolution is larger. Instead, we found that using the whole wavelength range can increase uncertainties due to severe template mismatches, likely due to the low ($S/N = 12$) average S/N of our spectra. Therefore, we chose to run *fxcor* on the region surrounding the Calcium Triplet (CaT) at 8498–8548–8662 Å, because these three lines occupy a very narrow wavelength range. Therefore, we correlate the scientific spectra between 8485–8750 Å with the template spectra between 8450–8720 Å. This means that we are able to measure the radial velocities of unresolved objects between -500 km s^{-1} and $+3000\text{ km s}^{-1}$, which include both Galactic stars and Fornax objects.

During the *fxcor* run, and prior to the correlation with the template spectra, the Fourier-transformed scientific spectra were filtered with a ramp filter. The filter was set up to cut off noisy high frequencies as well as low frequencies which may result from poor continuum fitting. The continuum was fitted with a cubic spline function. We ran *fxcor* in non-interactive mode, meaning that *fxcor* always returns the velocity corresponding to the highest cross-correlation with the template spectrum. The final radial velocity is the median of the single radial velocities obtained from the cross-

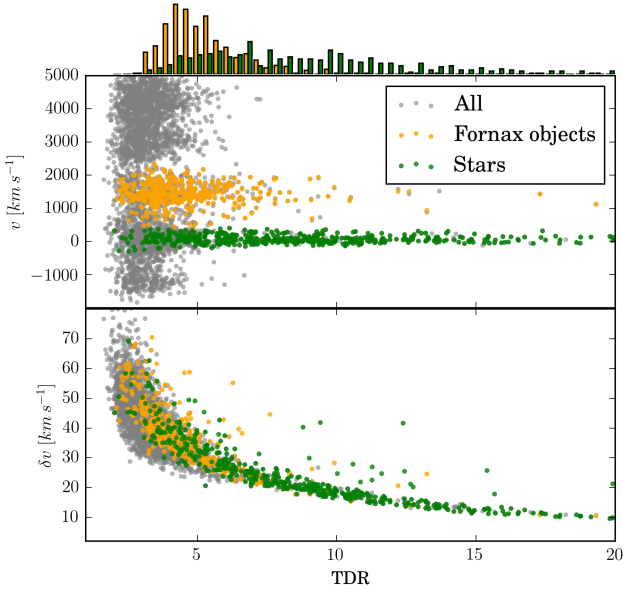


Figure 3. Results from *iraf/fxcor* for ~ 4200 spectra. The x-axis represents the Tonry & Davies R parameter (TDR) which is a proxy for the goodness of the cross-correlation between the scientific and the template spectra. Smaller TDR corresponds to larger velocity uncertainties δv (bottom panel) and therefore to a poorer spectral fit. The measured radial velocity v is shown on the y-axis of the top panel. The sequence of objects at $v \approx 0 \text{ km s}^{-1}$ are Galactic stars, whereas the cluster at $v \approx 1700 \text{ km s}^{-1}$ are sources in the Fornax cluster. The histogram on the top shows raw counts for stars and Fornax objects, respectively.

correlation with the 40 template stars. To overcome extreme template mismatch (i.e. the case in which the fitted radial velocity varies considerably depending on the adopted template), we used a median-absolute-deviation algorithm (MAD) to flag radial velocities deviating more than 5σ from the median of the radial velocities obtained from the 40 template stars. Outliers, if any, are removed from the velocity set and the final radial velocity and error are computed from the remaining measurements. 90 per cent of GCs and stars have between 0 to 5 outliers, suggesting that the effect of extreme template mismatch is small.

The scatter in radial velocity due to normal template mismatch (i.e. due to intrinsic mixture of stellar populations in GCs) varies between $3 - 10 \text{ km s}^{-1}$ (after removing outliers) depending on the S/N of the spectrum. The final error on the radial velocity is the median velocity error returned by *fxcor* summed in quadrature to the scatter due to normal template mismatch.

We used the Tonry & Davis (1979) R factor (TDR hereafter) to assess the goodness of the correlation between scientific spectra and template spectra. As expected, TDR is inversely proportional to the velocity uncertainties. This effect is shown in Figure 3, where TDR is shown as a function of the measured radial velocity v and velocity uncertainty δv . It is worth noting that *fxcor* was set to measure the Doppler shift of the CaT lines only for objects with radial velocities $-500 < v < 3000 \text{ km s}^{-1}$. This means that only radial velocities measured to be $-450 < v < 2500 \text{ km s}^{-1}$ are meaningful, whereas velocities outside this range are non-physical, and thus discarded as meaningless. Heliocentric velocity was computed with *iraf/rvcorrect* for each slit, and subtracted from all radial velocities.

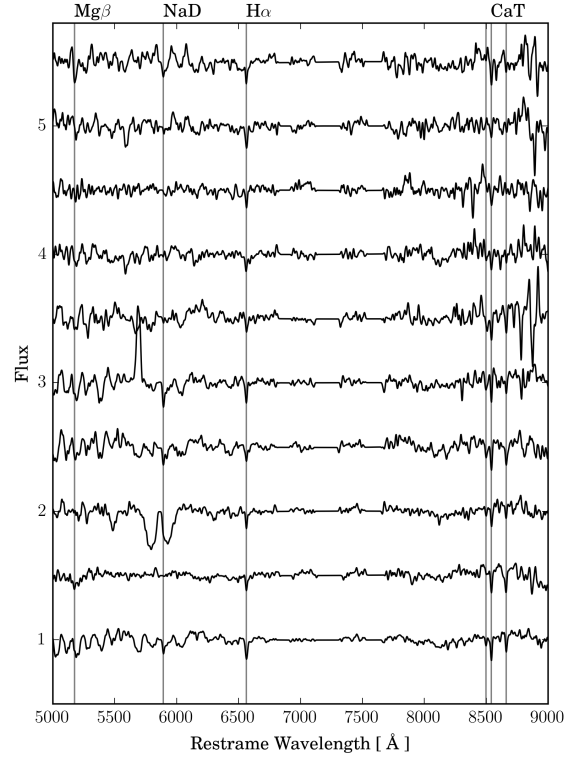


Figure 4. A sample of GC spectra suitably normalised. Shown are continuum-normalized redshift-corrected spectra for GCs with increasing S/N per resolution element (from top to the bottom). The spectrum at the top has $S/N = 15$, the one at the bottom $S/N = 50$. The main atomic lines are labelled on the top. Features such as the strong absorption in the spectrum at Flux = 2 and the emission in the spectrum at Flux = 3 are instrumental artifacts and not physical features of the GC. The flat horizontal lines between 7000–8000 Å mark regions with masked sky lines (see text).

3.2 Disentangling Fornax objects from foreground and background sources

We are interested in separating objects physically bound to the Fornax cluster (GCs, UCDs and galaxies) from objects unrelated to the Fornax cluster (Galactic stars and foreground or background galaxies). A first distinction can be performed on the basis of the systemic velocity. We use the same velocity range adopted by Schuberth et al. (2010) for GCs and Galactic stars. Using the top panel of Figure 3 as a reference, Fornax objects are those with $450 \leq v < 2500 \text{ km s}^{-1}$ (850 datapoints), whereas Galactic stars are those with $-450 < v < 450 \text{ km s}^{-1}$ (956 datapoints). The velocity determination of background galaxies and their distribution will be discussed in a separate paper.

Spectra of Fornax objects (GCs, UCDs) and Galactic star candidates were redshift-corrected and visually inspected. We checked for the correct positions of the following lines: CaT, H α (6563 Å), NaD(5892 Å), the Mg β triplet ($\sim 5175 \text{ Å}$) and H β (4861 Å). The CaT and H α lines, if present, are always visible, whereas the Mg β lines are hardly recognizable in spectra with $S/N \lesssim 10$. The NaD is not always visible because this atomic line is shifted onto a problematic sky line at 5860–5890 Å for spectra with $v \lesssim 1000 \text{ km s}^{-1}$.

. The H β line, at which the instrumental efficiency is less than 20 per cent, can be discerned only for spectra with $S/N \gtrsim 20$.

Figure 4 showcases some spectra with S/N ranging from 50 (bottom spectrum) to 15 (top spectrum). The GG475 filter of the first and third quadrant, coupled with the MR-grism, introduce an absorption feature between about $5600 < \lambda < 6300 \text{ \AA}$ (see the third spectrum from the bottom in Figure 4 for an example). This occurs because the GG475-filter is composed of 10–20% in its weight by sodium oxide. Impure manufacturing likely caused this feature but it does not affect our analysis because the blue part of the spectra is not used for our velocity measurements. Strong emission features can occasionally appear in the blue part of the spectra (see the fifth spectrum from the bottom in Figure 4), but they are attributed to zero order overlaps that are not corrected for by the Reflex reduction pipeline, rather than to physical phenomena associated with the light source.

For spectra with very low S/N the distinction between atomic lines and noise features becomes somewhat subjective. Therefore, all 850 Fornax object candidates were independently eyeballed by five members of the team. The inspection was performed on a dashboard including the 2D image of the source, the redshift corrected spectrum and attributes such as magnitude and S/N. We gave a vote of 1 to spectra which were certainly Fornax objects and 0 to non-Fornax object spectra. Votes from all members were summed-up for each spectrum. We found that 323 spectra received a vote of 5/5 (meaning that these spectra were classified as Fornax objects by all members of the team), 348 spectra received a vote $\geq 4/5$ and 420 spectra received a vote $\geq 3/5$. In the followings, we will use the last set of 420 spectra as our final spectroscopic catalogue of the Fornax cluster.

We repeated the above procedure to select a sample of spectroscopically confirmed Galactic stars with radial velocities in the range $-450 < v < +450 \text{ km s}^{-1}$, finding a total of 492 Galactic stars.

Of the total 4574 slits, we have allocated ~ 2400 slits on GC/UCD candidates, ~ 800 slits on background galaxies (selected via a star galaxy separation based on their colors and stellarity index from SExtractor), and ~ 1000 on stars. Schuberth et al. (2010) have already spectroscopically confirmed the brightest GCs in the central regions of NGC 1399 and we considered more valuable to focus on GC candidates not yet confirmed by previous studies, while still observing a few tens of known GCs to calibrate our velocity measurements against literature studies. The small recovery fraction we have obtained ($\sim 17\%$) is due to a number of factors: contamination from stars and background galaxies in the fainter end of the GC luminosities, low S/N objects due to their poor spectral quality (see Figure 3), and observation at large galactocentric radii where the GC density is below 1 GC/ arcmin 2 (see Figure 15 in Schuberth et al. 2010).

4 RESULTS

4.1 Velocity self-consistency

We measured radial velocities for 51 duplicated objects (including Galactic stars), observed across multiple VIMOS masks. The velocity difference Δv between duplicated objects is shown in Figure 5 as a function of g magnitude. We detected no clear trend between Δv and the magnitude, but a significant scatter is observed. One object has a velocity difference which scatters more than 3σ from the average. We attributed this disagreement to an issue with the wavelength calibration for this particular object. The root-mean-square

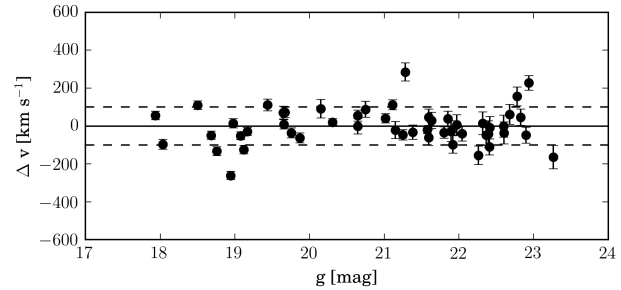


Figure 5. Internal velocity comparison. The figure shows the velocity difference Δv between GCs with two independent velocity measurements. The solid and dashed line represent the reference $\Delta v = 0 \text{ km s}^{-1}$ and $\Delta v = \pm 100 \text{ km s}^{-1}$, respectively.

of the velocity difference of GCs and stars combined is 91 km s^{-1} , which becomes 79 km s^{-1} after clipping the outlier. The former is our statistical error.

We weight-averaged the radial velocities of the duplicated GCs. This left us with a catalogue of 387 Fornax objects and 464 Galactic stars.

4.2 Comparison with literature data

The stellar systems surrounding NGC 1399 have been in the focus of many spectroscopic studies (Dirsch et al. 2004; Schuberth et al. 2010; Bergond et al. 2007; Firth et al. 2007; Chilingarian et al. 2011; Mieske et al. 2004; Hilker et al. 2007; Francis et al. 2012; Drinkwater et al. 2000).

To find which of our VIMOS objects have a literature counterpart, we matched our catalogue of 387 Fornax objects with the NED (Nasa/IPAC Extragalactic Database²) database using the *python/astropy* tools. We manually added the catalogue of Schuberth et al. (2010) to the literature database, because these GC measurements are not in NED. We required the literature objects to have a measured radial velocity and to be within 0.4 arcsec from our VIMOS source.

In most cases, the literature counterpart has been observed by more than one author. Table 1 reports the number of objects per author for which we have a VIMOS radial velocity. In order to compare literature velocities with our VIMOS velocities, we averaged together the radial velocities of unique objects observed in multiple literature studies. Overall, we found 48 of our Fornax objects to have a literature counterpart.

Figure 6 shows the comparison between our VIMOS objects and the unique literature objects obtained as explained above. No bias is detected. The root-mean-square of the velocity difference is 81 km s^{-1} .

4.3 Classification of Fornax objects

We classified all Fornax objects based on their morphology: namely GCs, ultra compact dwarfs (UCDs) and background galaxies. The spatial resolution of VST/OmegaCam is insufficient to resolve the typical half-light radii of GCs with $r_h < 10 \text{ pc}$ (Masters et al. 2010; Puzia et al. 2014). Although the size of UCDs with $r_h > 20 \text{ pc}$ can be resolved using our imaging data (Cantiello et al. 2015),

² <https://ned.ipac.caltech.edu/>

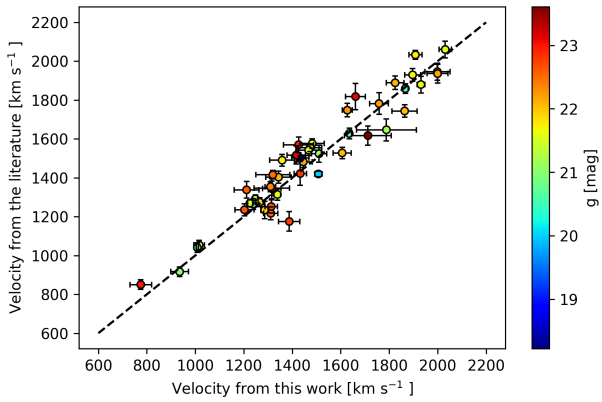


Figure 6. Comparison with literature studies. The radial velocity of literature objects is averaged among literature studies as discussed in the text. The 1-to-1 line is shown as a dashed line.

Paper	Number of duplicated objects
Dirsch et al. (2004)	29
Schuberth et al. (2010)	26
Bergond et al. (2007)	14
Firth et al. (2007)	11
Chilingarian et al. (2011)	2
Mieske et al. (2004)	1
Hilker et al. (2007)	1
Francis et al. (2012)	1
Drinkwater et al. (2000)	1

Table 1. Number of confirmed VIMOS objects also found in archival data grouped by author.

measuring UCD sizes is not the focus of this paper and will be deferred to a future work.

It is established that a sharp magnitude cut cannot perfectly separate UCDs from GCs. However, it has been shown (Voggel et al. 2016; Eigenthaler et al. 2018) that the bulk of candidate UCDs with confirmed sizes in the Fornax cluster have $M_V \leq -10$ ($\approx M_i \leq -11$). Therefore, we use this magnitude cut as benchmark value to separate UCDs with $i \leq 20.3$ from GCs with $i > 20.3$. This selection returns 15 UCD candidates and 372 likely GCs.

The object with coordinates RA(J2000) = 3:36:37.253 DEC(J2000) = 35:23:09.20 is the nucleus of the nucleated dwarf galaxy FCC 171, whose radial velocity was first measured in Bergond et al. (2007). This object will be included in the GC sample in the following analysis.

5 DISCUSSION

In this section we discuss some qualitative properties of the final dataset of bona-fide GCs and UCDs. We look at the spatial distribution and phase-space diagrams. A detailed kinematic and dynamic analysis (rotation curve, dark matter modelling, luminosity function analysis) will be the subject of forthcoming papers.

5.1 Phase-space and spatial distribution

The phase-space diagram and the spatial distribution are shown in Figure 7. In both cases, GCs, UCDs and Galactic stars are com-

pared to the catalogues of Bergond et al. (2007) and Schuberth et al. (2010). These two catalogues are the largest and most homogeneous in the literature. Moreover, the catalogue of Schuberth is an extension of the catalogue of Dirsch et al. (2004). Together they include sources within 18 arcmin from NGC 1399. Bergond et al.’s catalogue was designed to target intra-cluster globular clusters and it is more radially extended (see also Figure 1). It covers a strip of about 1.5 degree in right ascension and half a degree in declination. The catalogues of Schuberth et al. and Bergond et al. combined provide a good representation of the current archival phase-space and spatial distribution of the GC system in the core of the Fornax cluster.

The left panel in Figure 7 shows that the velocity distribution of GCs/UCDs is well separated from that of Galactic stars, although a few GCs between $10 < R < 20$ arcmin might be misclassified as Galactic stars.

The systemic velocity of GCs and UCDs is $v_{\text{GCs}} = 1443 \pm 18 \text{ km s}^{-1}$ and $v_{\text{UCDs}} = 1413 \pm 91 \text{ km s}^{-1}$, respectively. These are both consistent with the average systemic velocity from the literature $v_{\text{NED}} = 1425 \pm 4 \text{ km s}^{-1}$. Our sample also includes interlopers from large galaxies surrounding NGC 1399, in particular NGC 1380, NGC 1404, NGC 1387. The positions of these three galaxies in the phase-space diagram are also labelled.

It is not trivial to disentangle the GC population of NGC 1387 and NGC 1404 because of their proximity in phase-space to NGC 1399. Here we adopt a conservative approach to extract the GC system of these galaxies, but we acknowledge that more refined methodologies can return more accurate results, as we will discuss in forthcoming papers. Following Schuberth et al. (2010), we use 3 arcmin from the galaxy centre as a benchmark radius to select the bulk of GCs associated with these galaxies. We also require that the radial velocities of GCs have to be within $v_{\text{sys}} \pm 2\sigma$ the systemic velocity of the host galaxy, where σ is the galaxy stellar velocity dispersion. Here we used $\sigma = 247 \text{ km s}^{-1}$ (Vanderbeke et al. 2011), $v_{\text{sys}} = 1947 \text{ km s}^{-1}$ for NGC 1404 and $\sigma = 170 \text{ km s}^{-1}$ (Wegner et al. 2003), $v_{\text{sys}} = 1302 \text{ km s}^{-1}$ for NGC 1387, respectively.

After applying the above selection criteria, we found 17 and 8 GCs associated with NGC 1404 and NGC 1387, respectively. The larger number of GCs associated with NGC 1404 is due to the galaxy being more massive than NGC 1387, but also to its proximity to NGC 1399 which increases the fraction of contaminants. In the case of NGC 1380, with $\sigma = 190 \text{ km s}^{-1}$ (Vanderbeke et al. 2011) and $v_{\text{sys}} = 1877 \text{ km s}^{-1}$, the identification of its GC system is easier given its isolated position. Using the criteria above, we found 7 GCs associated with this galaxy.

The right panel of Figure 7 displays the spatial distribution of our GC and UCD catalogues. This diagram also shows how our catalogue is complementary to literature catalogues: it increases the object sampling in the central regions of the galaxy and it fills gaps without literature data in the outer regions.

GC systems which are bound to other giant galaxies can be seen clustered around their centres. Figure 7 suggests that our combined sample might also contain some GCs belonging to NGC 1379 and NGC 1381 (see Figure 1).

5.2 Photometric diagrams

Figure 8 displays the distribution of GCs/UCDs in the photometric space. These are compared with the distribution of all sources targeted for spectroscopic follow-up, including Galactic stars and background galaxies. Although the u filter is known to well discriminate GCs from contaminants, here we only consider g , r , i

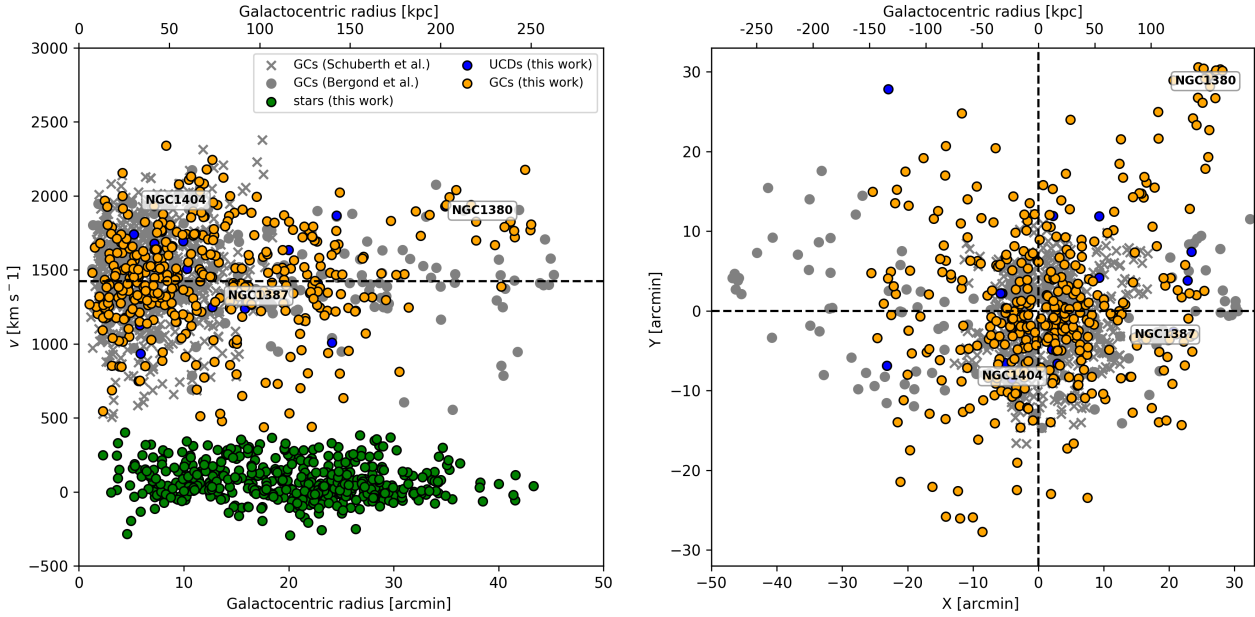


Figure 7. *Left:* Phase-space velocity diagram. The figure shows the measured systemic velocity of the Fornax objects presented in this paper (orange points), GCs from Schuberth et al. (2010) (grey crosses), GCs from Bergond et al. (2007) (grey points) and Galactic stars measured in this paper (green points). The systemic velocity of NGC 1399 is marked with a dashed line at $v = 1425$ km s $^{-1}$. The systemic velocity and galactocentric distance of giant Fornax galaxies (namely NGC 1404, NGC 1387, NGC 1380) are marked with the correspondent galaxy name. The distance is expressed in arcminutes from the centre of NGC 1399. Physical distances in kpc are also shown on the top panel. *Right:* Position diagram, with North to the top and East to the left. The plot shows the spatial distribution of the objects from the left panel (except for Galactic stars for clarity). Note how the GCs from our paper complement the GC catalogues of Schuberth et al. (2010) and Bergond et al. (2007).

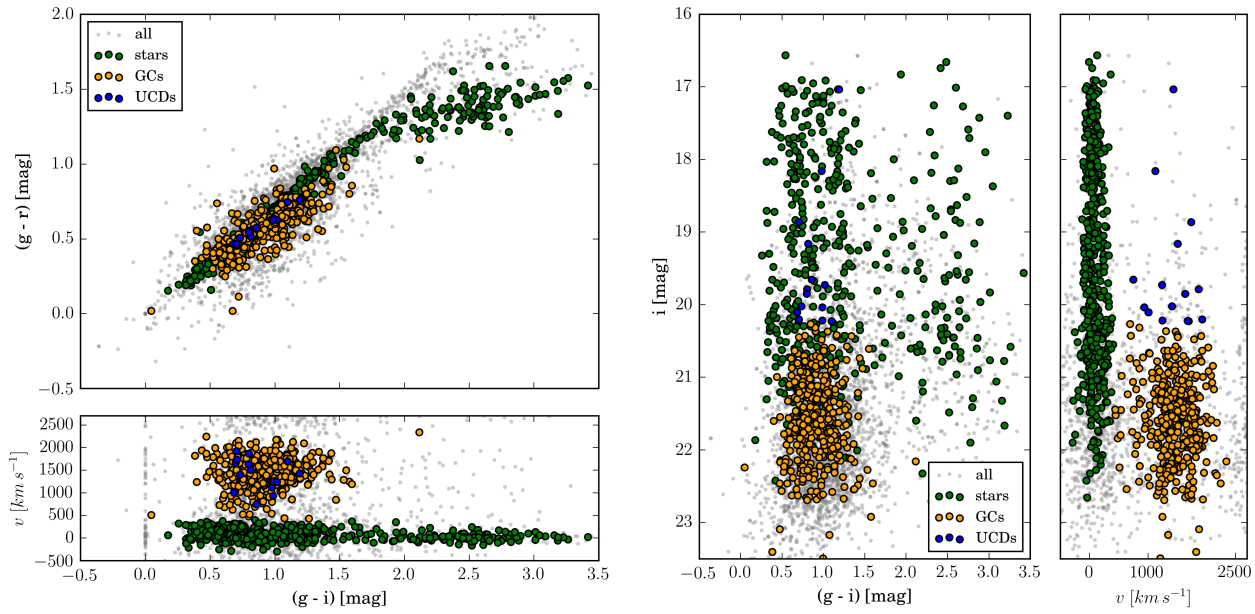


Figure 8. Colour–colour and colour–magnitude diagram. The figure shows the distribution of the labelled objects in a $(g - i)$ vs. $(g - r)$ space (left panel) and $(g - i)$ vs i space (right panel). Each diagram includes also a radial velocity v axis to show the separation of GCs/UCDs from stars and galaxies. The objects labelled as ‘all’ represent all 4340 sources observed with VIMOS.

magnitudes because all but one GCs/UCDs have a genuine measurement in these photometric bands, whereas only 50% of our GCs/UCDs have a FDS *u*-band measurement. This is due to FDS *u*-band imaging being shallower than the other bands for detecting faint GCs (D'Abrusco et al. 2016).

GCs/UCDs and contaminants are not well separated using merely *g*, *r*, *i* filters, but velocity information clearly separates GCs/UCDs from Galactic stars and background galaxies. This is also shown in Figure 8 (left-bottom panel with (*g* − *i*) vs *v*) which shows how the velocity dispersion of blue GCs with (*g* − *i*) ≤ 0.85 is higher than that of the red GCs, a property shared with GC systems in the most giant galaxies (e.g., Pota et al. 2013). The right-most panel, with *v* vs *i*, shows that the velocity distribution of all GCs has an extended tail towards lower velocities (a property also visible in Figure 7). This effect was already noticed in Schuberth et al. (2010). The convincing separation between GCs and stars also ensures that this property is unlikely due to miss-classified GCs.

5.3 Root-mean-square velocity profile

The root-mean-square velocity v_{rms} quantifies the total kinetic energy of a stellar system. It accounts both for the ordered and for the random stellar motions. Here we compute the root-mean-square velocity as:

$$v_{\text{rms}}^2 = \frac{1}{N} \sum (v_i - v_{\text{sys}})^2 - (\Delta v_i)^2, \quad (1)$$

where v_i is the radial velocity of the i -th GC and Δv_i is its uncertainty. $v_{\text{sys}} = 1425 \text{ km s}^{-1}$ is the systemic velocity of NGC 1399. Uncertainties were derived with the formulae provided by Danese et al. (1980). Statistical errors are discussed in Section 4.

The v_{rms} has been calculated using a total of 1133 unresolved objects (including GCs and UCDs). Although we cannot exclude that GCs and UCDs are decoupled populations, the fraction of classified UCDs is too modest to affect the overall average kinematics of the combined populations. A detailed analysis of UCDs is beyond the purpose of this paper, however, looking at Fig. 7, object classified as UCDs do not show any evident systematic difference with respect to the GC systems. The final catalogue is made of the 387 objects discussed in this paper combined with the catalogues of Bergond et al. (2007) and Schuberth et al. (2010). Our master catalogue includes GCs from other giant galaxies in the field. If an object was found in more than one catalogue we computed its weight-average radial velocity. Also, GCs and UCDs from literature catalogues were given the VST photometry discussed in this work. Therefore, no photometric calibration was required.

Figure 9 displays the v_{rms} profile for: i) our combined master catalogue of 1133 GCs and UCDs, including literature objects; ii) the GC catalogue of Schuberth et al. (2010), iii) the central stars of galaxies surrounding NGC 1399; iv) all Fornax galaxies from Drinkwater et al. (2000), v) PN from FVSS-II (Spinelli et al. 2018, submitted). The v_{rms} profile is computed in radial bins of irregular size. However, each bin contains roughly the same number of objects, namely: 48, 66, 88 objects per bin for the blue, red and all GCs (including UCDs), respectively.

The master catalogue contains GCs and UCDs predominantly from NGC 1399, which is the largest and most massive system in the field dominating the total potential in the core of the cluster. Here, objects from other galaxies, embedded in the extended exponential halo around the galaxy (Iodice et al. 2016), in particular NGC 1404, NGC 1387, are likely to contaminate the kinematics of the central galaxy. However, looking at the v_{rms} profile of the

total sample (shaded gray area) there is a steep rise in the profile around $R \sim 10$ arcmin (~ 50 Kpc) which marks a kinematical transition from a “colder” kinematical region to a “warmer” one. The same behavior can be observed in the PNs datapoints (magenta triangles). As discussed in FVSS-II, the peak in v_{rms} of the point around $R \sim 8$ arcmin, could partially be due to NGC 1404. In fact, Planetaryes bounded to this galaxy could possibly contaminate the sample, causing an increase of the v_{rms} in that particular radial bin.

Regarding the data form Schuberth et al., we use their full data dataset (corresponding to sample BI and RI in their Table A.1) because its properties are akin to those of our master catalogue. The v_{rms} profile is in general agreement for the red GCs, but we observe a disagreement for blue GCs in the region $5 < R < 10$ arcmin, where the data from Schuberth et al. are systematically higher than our datapoints. Such a discrepancy might be due to the different colour threshold used for the blue/red separation: we use $(g - i) = 0.85$ mag, whereas Schubert et al. use $(g - i) = 0.91$ mag (after converting their Washington magnitudes to SDSS magnitudes). Also, we applied no magnitude cut before calculating the v_{rms} , whereas Schubert et al. only considered GCs brighter than $R > 21.1$ mag.

In the outermost region, the v_{rms} profile flattens out to a value which is fairly consistent with the kinematics of the cluster galaxies (the green data point at $R \sim 35$ arcmin from Drinkwater et al. 2000). This suggests that the GC kinematics at radii $R > 10$ arcmin is ruled by the cluster potential. This feature demonstrates that the photometric transition radius between the bright central galaxy and the outer exponential halo at $R \sim 10$ arcmin from Iodice et al. (2016) represents the radius where we kinematically observe the emergence of an intracluster population of GCs and PNe. At the light of similar conclusions found for PNs by Spinelli et al. (2018, submitted), there is growing evidence that multiple independent lines of investigation are starting to support, for the first time, the existence of a photometrically and kinematically distinct intracluster component in the Fornax Cluster core.

When split in the red and blue subpopulations, using a colour cut at $(g - i) = 0.85$ mag the GC sample shows some interesting differences. At all radii the v_{rms} profile of the red GCs is systematically smaller than the one of the blue GCs, albeit the two profiles are broadly consistent with each other within one sigma. The v_{rms} of PNs is consistent with that of red GCs, as observed in most giant galaxies (e.g., Pota et al. 2013). In the innermost regions at $R < 10$ arcmin our results are consistent with those from Schuberth et al. (2010). In particular the blue GCs turn out to be the more extended population in radius, nicely connecting to the value of the cluster galaxy datapoint. The difference in normalisation between the two populations may be driven by the different slopes of the two populations’ density profiles as measured, e.g., by Schuberth et al. (2010, their Eq. 10 and 11 and Table 5).

Finally, we report in the same Figure the central velocity dispersions of the giant galaxies populating the same area occupied by the total GC catalogue (see Figure 1). For NGC 1399, we show long slit data from Saglia et al. (2000) up to 1 arcmin galactocentric radius, where the stellar velocity dispersion is consistent with the velocity dispersion of the innermost GCs. At larger distances one can expect that neighbouring galaxies might contaminate the overall GC kinematics. Especially in the outer regions, i.e. $R > 10$ arcmin, assuming these regions are dominated by the cluster potential, the presence of GCs bound to the galaxies might alter the true intracluster population. A detailed separation of the bound GC population from the true intra-cluster GCs (unbound from any galaxy in the core) will be addressed in a forthcoming paper.

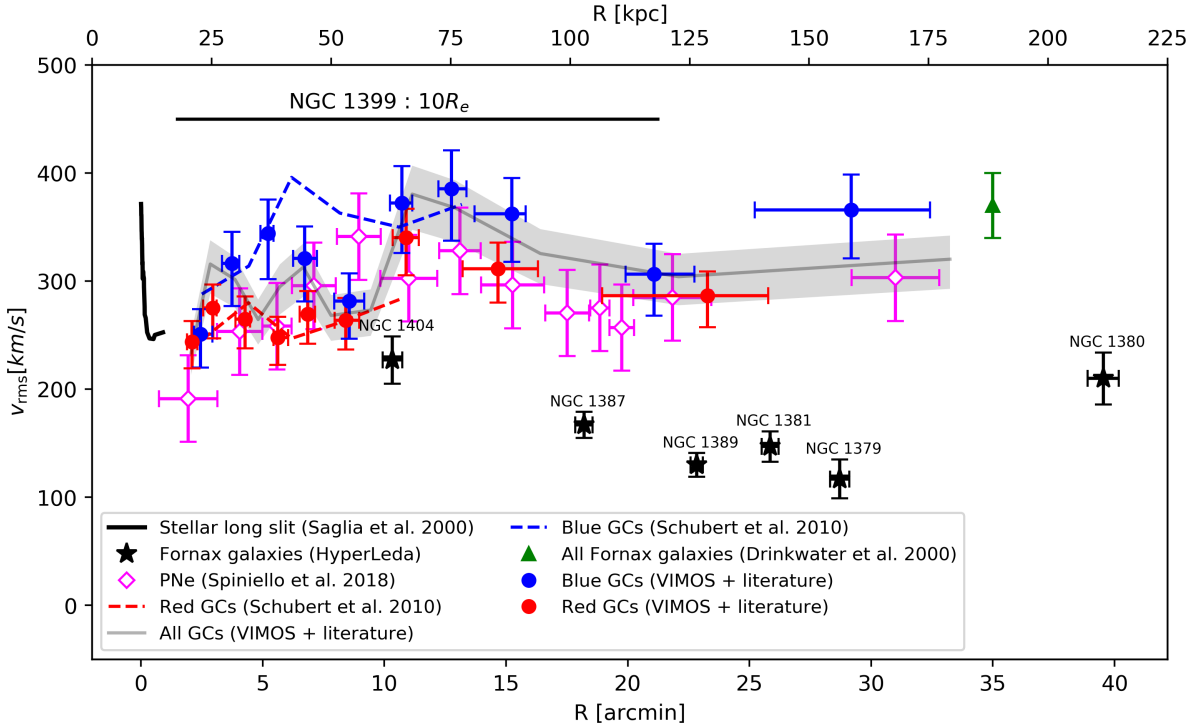


Figure 9. Root-mean-square velocity dispersion of NGC 1399 stellar system. The blue and red points represent the blue and red GCs/UCDs, respectively, whereas the full grey-line shows the full master catalogue of 1133 GCs/UCDs. Bins are of irregular size, reflected in the asymmetric radial error bars representing the 25-th and 75-th quantiles. The digitised v_{rms} profiles from Schubert et al. (2010) are the blue and red dashed lines, without uncertainties for clarity. The central stellar velocity dispersion for the galaxies in the field are the black points, with the error bars on the x-axis representing one effective radius. The green triangle shows the innermost value of the velocity dispersion derived for Fornax galaxies by Drinkwater et al. (2000).

In conclusion of this section, we can summarise the main finding of this paper in Figure 9, by saying that the unprecedented extension of the GC kinematics, combined with the literature data, has demonstrated the kinematical signature of a population of intracluster GCs, made of both red GCs and blue GCs. The two populations show v_{rms} profiles consistent with the transition of GC dynamics driven by the potential of the central giant elliptical in Fornax (NGC 1399) in the innermost regions to GC dynamics governed by the cluster potential beyond ~ 10 arcmin (~ 50 kpc) galacto-centric distance.

Analogous signatures of intracluster stellar populations have been shown previously in the Virgo, Fornax and Coma clusters (see e.g., Paolillo et al. 2002; Arnaboldi et al. 2004; Peng et al. 2011; Longobardi et al. 2015) but the catalog presented here will offer a unique chance to perform a fully dynamical analysis of both the bound and unbound GC populations (D'Abrusco et al. 2016).

6 CONCLUSIONS

In this paper, we presented the results of a wide 1 deg^2 spectroscopic survey of GCs in the Fornax cluster, focusing on observations, data reduction and presentation of the final catalogue. This is the first work of a larger multi-instrument program dubbed the Fornax Cluster VLT Spectroscopic Survey (FVSS), which, in synergy with the ongoing Fornax Deep Survey (FDS), aims to study the formation, evolution and dynamics of galaxies and small stellar systems in the Fornax cluster.

Our analysis is based on observations with VST/OmegaCam

for imaging and 25 VST/VIMOS masks for spectroscopic follow-up. Objects were pre-selected with multi-band imaging based on optical FDS and near-infrared NGFS photometry, supported also by the many spectroscopic catalogues already present for this region of the sky. Approximately 4500 objects were observed. The total observation time was 37.5 hours, mostly in sub-arcsec seeing conditions. Data reduction was performed using the ESO VIMOS pipeline. Redshifts were extracted using *iraf/fxcor*, whereas the remaining data analysis was carried out using customer *python* code. Only the Calcium Triplet region (8498 to 8662 Å) was used for redshift estimation, but the quality of the fit was assessed using the full spectrum from 4800 to 10000 Å.

After a visual inspection of candidate spectra, we compiled a consensus catalogue of 372 GCs, 15 UCDs (objects with $i \leq 20.3$ mag) and 464 Galactic stars. Most GCs belong to the dominant galaxy NGC 1399, but we estimated that 30–40 objects might belong to NGC 1404, NGC 1380, and to other major galaxies in the observed field.

We have used the new complete catalog of GCs to derive the total v_{rms} of the GC sample and also split the sample in red and blue subsamples using the threshold $(g - i) = 0.85$ mag. We have demonstrated that all profiles show a similar signature at around $R \sim 10$ arcmin of a kinematical transition from a low v_{rms} regime ($\sim 250 \text{ km s}^{-1}$) to a higher one ($\sim 350 \text{ km s}^{-1}$), with the former being consistent with the central velocity dispersion of NGC 1399 (the central cluster galaxy) and the latter being consistent with the velocity dispersion of the Fornax cluster galaxy population. This demonstrates that at $R > 10$ arcmin both GC populations feel

strongly the cluster potential, rather than the increasingly weaker galaxy potential galaxy potential. Parallel to this paper we also performed a similar analysis where we present similar evidence based on kinematical distribution of planetary nebulae (PNe) in the core of the cluster, up to 200 Kpc (Spiniello et al. 2018, submitted). PNe also show a rise in the velocity dispersion compatible with PNe tracing the potential of the cluster as a whole. A detailed kinematical characterization of these intra cluster populations will be the topic of a forthcoming analysis. We point out here that both lines of kinematical evidence (GCs and PNe) corroborate the photometric evidence, found in the deep galaxy photometry, of a transition region between the bright central galaxy and the outer exponential halo at $R \sim 10$ arcmin from Iodice et al. (2016) and show, from the dynamical point of view, the emergence of an intracluster population of GCs (as well as PNe) in the Fornax galaxy Cluster.

ACKNOWLEDGMENTS

NRN and EI acknowledge financial support from the European Union's Horizon 2020 research and innovation programme under the Marie Skłodowska-Curie grant agreement No 721463 to the SUNDIAL ITN network and PRIN INAF 2014 "Fornax Cluster Imaging and Spectroscopic Deep Survey". CT is supported through an NWO-VICI grant (project number 639.043.308). CSpiniello has received funding from the European Union's Horizon 2020 research and innovation programme under the Marie Skłodowska-Curie actions grant agreement No 664931. M.P. acknowledges financial contribution from the agreement ASI-INAF No 2017-14-H.O. T.L. acknowledges financial support from the European Union's Horizon 2020 research and innovation programme under the Marie Skłodowska-Curie grant agreement No. 721463 to the SUNDIAL ITN network. P.E. acknowledges support from the Chinese Academy of Sciences (CAS) through CAS-CONICYT Postdoctoral Fellowship CAS150023 administered by the CAS South America Center for Astronomy (CASSACA) in Santiago, Chile. MS acknowledge financial support from the VST project (P.I. P. Schipani). The authors acknowledge financial support from the European Union's Horizon 2020 research and innovation programme under Marie Skłodowska-Curie grant agreement No 721463 to the SUNDIAL ITN network. GvdV acknowledges funding from the European Research Council (ERC) under the European Union's Horizon 2020 research and innovation programme under grant agreement No 724857 (Consolidator Grant ArcheoDyn). R.D'A. is supported by NASA contract NAS8-03060 (Chandra X-ray Center). THP acknowledges support by the FONDECYT Regular Project No. 1161817 and the BASAL Center for Astrophysics and Associated Technologies (PFB-06). This research made use of Astropy, a community-developed core Python package for Astronomy (Astropy Collaboration, 2018)

REFERENCES

- Arnaboldi M., Gerhard O., Aguerri J. A. L., Freeman K. C., Napolitano N. R., Okamura S., Yasuda N., 2004, *ApJ*, 614, L33
- Arnaboldi M., Ventimiglia G., Iodice E., Gerhard O., Coccato L., 2012, *A&A*, 545, A37
- Bassino L. P., Richtler T., Dirsch B., 2006, *MNRAS*, 367, 156
- Bergond G., Athanassoula E., Leon S., Balkowski C., Cayatte V., Chemin L., Guzmán R., Meylan G., Prugniel P., 2007, *A&A*, 464, L21
- Bottini D., Garilli B., Maccagni D., Tresse L., Le Brun V., Le Fèvre O., Picat J. P., Scaramella R., Scoggio M., Vettolani 2005, *PASP*, 117, 996
- Bullock J. S., Johnston K. V., 2005, *ApJ*, 635, 931
- Cantiello M., Capaccioli M., Napolitano N., Grado A., Limatola L., Paolillo M., Iodice E., Romanowsky A. J., Forbes D. A., Raimondo G., Spavone M., La Barbera F., Puzia T. H., Schipani P., 2015, *A&A*, 576, A14
- Cantiello M., D'Abrusco R., Spavone M., Paolillo M., Capaccioli M., Limatola L., Grado A., Iodice E., Raimondo G., Napolitano N., Blakeslee 2017, ArXiv e-prints
- Capaccioli M., Spavone M., Grado A., Iodice E., Limatola L., Napolitano N. R., Cantiello M., Paolillo M., Romanowsky A. J., Forbes D. A., Puzia T. H., Raimondo G., Schipani P., 2015, *A&A*, 581, A10
- Cappellari M., Emsellem E., 2004, *PASP*, 116, 138
- Chilingarian I. V., Mieske S., Hilker M., Infante L., 2011, *MNRAS*, 412, 1627
- D'Abrusco R., Cantiello M., Paolillo M., Pota V., Napolitano N. R., Limatola L., Spavone 2016, *ApJ*, 819, L31
- Danese L., de Zotti G., di Tullio G., 1980, *A&A*, 82, 322
- Dirsch B., Richtler T., Geisler D., Gebhardt K., Hilker M., Alonso M. V., Forte J. C., Grebel E. K., Infante L., Larsen S., Minniti D., Rejkuba M., 2004, *AJ*, 127, 2114
- Drinkwater M. J., Gregg M. D., Colless M., 2001, *ApJ*, 548, L139
- Drinkwater M. J., Phillipps S., Jones J. B., Gregg M. D., Deady J. H., Davies J. I., Parker Q. A., Sadler E. M., Smith R. M., 2000, *A&A*, 355, 900
- Duc P.-A., Cuillandre J.-C., Alatalo K., Blitz L., Bois M., Bournaud F., Bureau M., Cappellari M., Côté P., Davies R. L., Davis 2011, in Carignan C., Combes F., Freeman K. C., eds, Tracing the Ancestry of Galaxies Vol. 277 of IAU Symposium, Investigating the Merger Origin of Early-type Galaxies using Ultra-deep Optical Images. pp 238–241
- Eigenthaler P., Puzia T. H., Taylor M. A., Ordenes-Briceño Y., Muñoz R. P., Ribbeck K. X. a., 2018, ArXiv e-prints
- Ferguson H. C., Sandage A., 1989, *ApJ*, 346, L53
- Firth P., Drinkwater M. J., Evstigneева E. A., Gregg M. D., Karick A. M., Jones J. B., Phillipps S., 2007, *MNRAS*, 382, 1342
- Francis K. J., Drinkwater M. J., Chilingarian I. V., Bolt A. M., Firth P., 2012, *MNRAS*, 425, 325
- Freudling W., Romaniello M., Bramich D. M., Ballester P., Forchi V., García-Dabló C. E., Moehler S., Neeser M. J., 2013, *A&A*, 559, A96
- Grillmair C. J., Freeman K. C., Bicknell G. V., Carter D., Couch W. J., Sommer-Larsen J., Taylor K., 1994, *ApJ*, 422, L9
- Hilker M., Baumgardt H., Infante L., Drinkwater M., Evstigneeva E., Gregg M., 2007, *A&A*, 463, 119
- Iodice E., Capaccioli M., Grado A., Limatola L., Spavone M., Napolitano N. R., Paolillo M., Peletier R. F., Cantiello M., Lisker T., Wittmann C., Venhola A., Hilker M., D'Abrusco R., Pota V., Schipani P., 2016, *ApJ*, 820, 42
- Iodice E., Spavone M., Cantiello M., D'Abrusco R., Capaccioli M., Hilker M., Mieske S., Napolitano N. R., Peletier R. F., Limatola L., Grado A., Venhola A., Paolillo M., Van de Ven G., Schipani P., 2017, *ApJ*, 851, 75
- Jordán A., Blakeslee J. P., Côté P., Ferrarese L., Infante L., Mei S., Merritt D., Peng E. W., Tonry J. L., West M. J., 2007, *ApJS*, 169, 213
- Le Fèvre O., Saisse M., Mancini D., Brau-Nogue S., Caputi O., Castinel L., D'Odorico S., Garilli B., Kissler-Patig M., Lucuix C., Mancini G., Pauget A., Sciarretta G., Scoggio M., Tresse

- L., Vettolani G., 2003, in Iye M., Moorwood A. F. M., eds, Instrument Design and Performance for Optical/Infrared Ground-based Telescopes Vol. 4841 of Proc. SPIE, Commissioning and performances of the VLT-VIMOS instrument. pp 1670–1681
- Longobardi A., Arnaboldi M., Gerhard O., Hanuschik R., 2015, *A&A*, 579, A135
- Masters K. L., Jordán A., Côté P., Ferrarese L., Blakeslee J. P., Infante L., Peng E. W., Mei S., West M. J., 2010, *ApJ*, 715, 1419
- Mentz J. J., La Barbera F., Peletier R. F., Falcón-Barroso J., Lisker T., van de Ven G., Loubser S. I., Hilker M., Sánchez-Janssen 2016, *MNRAS*, 463, 2819
- Mieske S., Hilker M., Infante L., 2004, *A&A*, 418, 445
- Muñoz R. P., Eigenthaler P., Puzia T. H., Taylor M. A., Ordenes-Briceño Y., Alamo-Martínez 2015, *ApJ*, 813, L15
- Muñoz R. P., Puzia T. H., Lançon A., Peng E. W., Côté P., Ferrarese 2014, *ApJS*, 210, 4
- Murante G., Giovalli M., Gerhard O., Arnaboldi M., Borgani S., Dolag K., 2007, *MNRAS*, 377, 2
- Napolitano N. R., Arnaboldi M., Capaccioli M., 2002, *A&A*, 383, 791
- Napolitano N. R., Pannella M., Arnaboldi M., Gerhard O., Aguerri J. A. L., Freeman K. C., Capaccioli M., Ghigna S., Governato F., Quinn T., Stadel J., 2003, *ApJ*, 594, 172
- Paolillo M., Fabbiano G., Peres G., Kim D.-W., 2002, *ApJ*, 565, 883
- Peng E. W., Ferguson H. C., Goudfrooij P., Hammer D., Lucey J. R., Marzke R. O., Puzia T. H., Carter D., Balcells M., Bridges T., Chiboucas 2011, *ApJ*, 730, 23
- Pota V., Forbes D. A., Romanowsky A. J., Brodie J. P., Spitler L. R., Strader J., Foster C., Arnold J. A., Benson A., Blom C., Hargis J. R., Rhode K. L., Usher C., 2013, *MNRAS*, 428, 389
- Puzia T. H., Paolillo M., Goudfrooij P., Maccarone T. J., Fabbiano G., Angelini L., 2014, *ApJ*, 786, 78
- Rudick C. S., Mihos J. C., McBride C., 2006, *ApJ*, 648, 936
- Saglia R. P., Kronawitter A., Gerhard O., Bender R., 2000, *AJ*, 119, 153
- Scharf C. A., Zurek D. R., Bureau M., 2005, *ApJ*, 633, 154
- Schipani P., Capaccioli M., D’Orsi S., Marcozzi C., Marty L., De Paris G., Fierro D., Arcidiacono C., Farinato J., Magrin D., Ragazzoni R., Umbrico G., Brescia M., Molfese C., Perrotta F., Ferragina L., 2012, Memorie della Società Astronomica Italiana Supplementi, 19, 393
- Schuberth Y., Richtler T., Hilker M., Dirsch B., Bassino L. P., Romanowsky A. J., Infante L., 2010, *A&A*, 513, A52
- Strader J., Romanowsky A. J., Brodie J. P., Spitler L. R., Beasley M. A., Arnold J. A., Tamura N., Sharples R. M., Arimoto N., 2011, *ApJS*, 197, 33
- Sutherland W., Emerson J., Dalton G., Atad-Ettedgui E., Beard S., Bennett R., Bezwada N., Born A., Caldwell M., Clark P., Craig S., Henry 2015, *A&A*, 575, A25
- The Astropy Collaboration Price-Whelan A. M., Sipőcz B. M., Günther H. M., Lim P. L., Crawford S. M., Conseil S., Shupe D. L., Craig M. W., Dencheva 2018, ArXiv e-prints
- Tonry J., Davis M., 1979, *AJ*, 84, 1511
- Tonry J. L., Dressler A., Blakeslee J. P., Ajhar E. A., Fletcher A. B., Luppino G. A., Metzger M. R., Moore C. B., 2001, *ApJ*, 546, 681
- Valdes F., Gupta R., Rose J. A., Singh H. P., Bell D. J., 2004, *ApJS*, 152, 251
- Vanderbeke J., Baes M., Romanowsky A. J., Schmidtobreick L., 2011, *MNRAS*, 412, 2017
- Venholo A., Peletier R., Laurikainen E., Salo H., Lisker T., Iodice E., Capaccioli M., Kleijn G. V., Valentijn E., Mieske S., Hilker M., Wittmann C. a., 2017, *A&A*, 608, A142
- Vogel K., Hilker M., Richtler T., 2016, *A&A*, 586, A102
- Wegner G., Bernardi M., Willmer C. N. A., da Costa L. N., Alonso M. V., Pellegrini P. S., Maia M. A. G., Chaves O. L., Rité C., 2003, *AJ*, 126, 2268